Journal Name

ARTICLE TYPE

Cite this: DOI: 10.1039/xxxxxxxxxx

Shear rate dependent margination of sphere-like, oblate-like and prolate-like micro-particles within blood flow †

Huilin Ye,[a] Zhiqiang Shen,[a] and Ying Li[a,b‡]

Received Date
Accepted Date

DOI: 10.1039/xxxxxxxxxx

www.rsc.org/journalname

This study investigates the shear rate dependent margination of micro-particles (MPs) with different shapes in blood flow through numerical simulations. We develop a multiscale computational model to handle the fluid-structure interactions involving in the blood flow simulations. Lattice Boltzmann method (LBM) is used to solve the plasma dynamics and a coarse-grained model is employed to capture the dynamics of red blood cells (RBCs) and MPs. These two solvers are coupled together by immersed boundary method (IBM). The shear rate dependent margination of sphere MP is firstly investigated. We find that margination of sphere MP dramatically increases with the increment of wall shear rate $\dot{\gamma}_\omega$ under 800 s^{-1}, induced by the broken of rouleaux in blood flow. However, the margination probability only slowly grows when $\dot{\gamma}_\omega > 800\ s^{-1}$. Furthermore, the shape effect of MPs are examined by comparing the margination behaviors of sphere-like, oblate-like and prolate-like MPs under different wall shear rates. We find that the margination of MPs is governed by the interplay of two factors: hydrodynamic collisions with RBCs including collision frequency and collision displacement of MPs, and near wall dynamics. MPs that demonstrate poor performance in one process such as collision frequency may stand out in the other process like near wall dynamics. Specifically, the ellipsoidal MPs (oblate and prolate) with small aspect ratio (AR) outperform those with large AR regardless of the wall shear rate, due to their better performance in both the collision with RBCs and near wall dynamics. Additionally, we find there exists a transition shear rate region $700\ s^{-1} < \dot{\gamma}_\omega < 900\ s^{-1}$ for all of these MPs: the margination probability dramatically increases with shear rate below this region and slowly grows above this region, similar to sphere MPs. We further use surface area to volume ratio (SVR) to distinguish different shaped MPs and illustrate their shear rate dependent margination in a contour on shear rate-SVR plane. It is of significance that we can approximately predict the margination of MPs with specific SVR. All these simulation results can be potentially applied to guide the design of micro-drug carriers for biomedical applications.

1 Introduction

Micro-particles (MPs) play important roles in the delivery of therapeutics and imaging agents in biomedical fields such as cancer treatment and magnetic resonance imaging[1–5]. During the circulation of MPs in blood flow, margination, defined as the migration from center of blood stream towards the vessel wall, is the first step for MPs to reach tumor sites. It is also crucial for the occurrence of subsequent processes, namely adhesion of MPs on the endothelial cells and their transmigration across the endothelial wall. However, the efficacy of MPs can be dramatically reduced by a number of biophysical barriers such as cellular uptake by immune cells[6] and degradation by protein absorption (opsonization)[7] during the blood circulation. Therefore, the design, synthesis and modification of MPs have attracted a lot of attention, aiming to maximize their margination towards biological targets by overcoming biophysical barriers.

The past two decades have witnessed significant advances in the optimal design of nano- and micro-particles as drug carriers[1,5,8–11]. It has been recognized that the geometrical features of MPs is one of the key design parameters[12–14]. The typical MP shape includes sphere-like (sphere and cubic), oblate-like (disc and oblate) and prolate-like (rod and prolate), which we con-

[a] Department of Mechanical Engineering, University of Connecticut, 191 Auditorium Road, Unit 3139, Storrs, Connecticut 06269, United States. Email: yingli@engr.uconn.edu; Fax: +1 860 4865088; Tel: +1 860 4867110.
[b] Institute of Materials Science, University of Connecticut, 97 North Eagleville Road, Unit 3136, Storrs, Connecticut 06269, United States.

† Electronic Supplementary Information (ESI) available: Simulation parameters and additional results for shear rate dependent margination of MPs.

sidered in this study. A number of relevant efforts have been dedicated to understand the margination of different shaped MPs under flowing conditions. For instance, in the absence of red blood cells (RBCs), nonspherical particles (discoidal particle [15] and rod particle [16]) are found to marginate more readily than spherical and hemispherical counterparts. Further theoretical analysis confirmed that discoidal particles showed largest propensity to marginate in a linear laminar flow [17]. In the real blood flow, margination of MPs should be influenced by the existence of RBCs [18,19]. Tokarev *et al.* [20] proposed a mathematical model to predict the margination of platelets within blood flow, which was attributed to the frequency of near-wall rebounding collisions with RBCs. In the *in vivo* experiments, discoidal particles were observed to accumulate more than others in most of the human organs [21]. Further experiments conducted by van de Ven *et al.* [22] revealed that disk-like MPs demonstrated higher accumulation at the near wall region of tumor sites compared to other shaped MPs. These evidences clearly demonstrate the nonspherical particle outperforms spherical counterpart in terms of localization on the wall.

However, the studies mentioned above cannot tell whether oblate-like or prolate-like MPs demonstrate superior performance as drug carriers. Furthermore, it should be emphasized that in many simulations and experiments, the margination is usually measured based on the counting of number of MPs adhered on the walls. For example, Thompson *et al.* [23] found that rod MPs displayed improved margination compared to spheres of equal volume. This result is based on the counting of MPs binding on the walls. Obviously, the margination and adhesion are two separate processes which are not easy to be differentiated in experimental studies. MPs that performs better in one of the processes cannot ensure their better performance in the other one. Vahidkhah and Bagchi [24] investigated these two processes separately. They found that oblate particles of moderate aspect ratio showed the highest near wall accumulation, and the prolate MPs performed the worst in the margination process. While in the adhesion process, the oblate particles had strongest adhesion, and the sphere MP is the worst. Though only considering the margination process, the shape dependence of MPs on margination behavior is very complicated. For instance, Reasor *et al.* [25] found that spherical MPs showed higher margination than that of disk-like ones such as oblate in their computation study. This is inconsistent with the results presented in Vahidkhah and Bagchi [24]. Also, in both simulation [26] and experiment [23], it was found that sphere MP indeed showed higher accumulation than rod-like (prolate) MP.

One of the major reasons for above discrepancy may be the flow conditions. From simulations to experiments, the flow condition like shear rate varies by one or two orders of magnitude. Tilles and Eckstein [27,28] observed that the accumulation of platelet-sized MPs strongly depended on the wall shear rate of the flow, and they found a critical wall shear rate under which there is no significant accumulation of MPs. Besides, Gentile *et al.* [15] found that the margination dynamics of MPs with different shapes manifested different dependences on the shear rate of flow. The influence of flow condition was further confirmed by Muller *et al.* [26]: when increasing the shear rate of the flow, the difference of margination between sphere and prolate would become smaller.

Hence, present study further explores the shear rate effect on the margination of different shaped MPs in blood flow from pure hydrodynamic perspective, without considering the near wall adhesion. We develop a multiscale computational model to study the margination behavior of sphere-like, oblate-like and prolate-like MPs in the blood flow, which is modeled as a suspension of RBCs within blood plasma. The margination probability is adopted to quantify the margination behaviors of different shaped MPs. We find that the margination dynamics of MPs are governed by their collision with RBCs and near wall motion. The shear rate influences the margination dynamics through affecting the collision frequency, collision displacement and near wall motion. Furthermore, we find that all the different shaped MPs have the same trend of shear rate dependent margination. For the differences in margination probabilities of different shaped MPs, we can explain them reasonably well by comparing the collision and near wall motion. Lastly, we create a contour plot for the margination probability of different shaped MPs on the shear rate-surface area to volume ratio (SVR) plane. It provides the direct guidance for the optimal design of MPs by maximizing their margination.

This work is organized as follows. Section 2 identifies the physical problem of MPs transport in blood flow and numerical methods we employ to solve fluid flow and particle dynamics. Section 3 presents the margination results, and a detailed discussion of different physical mechanisms is proposed. In Section 4, concluding remarks are given.

2 Computational Model and Numerical Method

2.1 Physical problem

The blood flow is mainly consisted by RBCs and plasma. Other components such as white blood cell (also namely leukocyte) and platelets are not considered here due to their low volume fraction ($\sim 1\%$). In the normal human blood vessel, the occupation of RBCs (hematocrit) is about 45% in volume fraction. Although the plasma contains protein, glucose and mineral ions, 92% by volume of it is water. So, it is usually considered as a Newtonian fluid. The MPs carrying drug molecules will move with the bulk flow after they are intravenously injected into blood vessel. There are two typical while opposite motions happening in blood flow. The first is the migration of RBCs away from vessel wall. This cross-stream migration is induced by the deformation of RBCs. Due to the existence of wall, deformed RBCs break up the symmetry of Stokes flow (Reynolds number of blood flow in venule or vein is usually about $O(10^{-6} \sim 10^{-3})$) and experience a lift force guiding them to move away. This migration of RBCs results in the formation of a cell-free layer (CFL) near the vessel wall, in which there is no RBCs. Also, it leads to RBC-rich layer in the center region of channel. The famous Fahraeus-Lindqvist effect [29] is caused by the CFL which acts as a lubricant layer to reduce the blood flow resistance. Comparing with the migration of RBCs, the other typical motion in blood flow is the margination of stiff or rigid particles, including white blood cells, nano- and micro-

drug carriers. Together with the shear stress exerted by the flow, the interaction between MPs and RBCs such as collision drive the MPs to move towards the vessel wall.

To systematically investigate the margination behaviors of MPs under the interplay of shape and shear rate, we conduct 64 simulations in total. Here, 8 different wall shear rates ranging from 200 s^{-1} to 2000 s^{-1} are considered. This regime locates within the normal physiological flow environment from venules to capillaries[30]. We consider 8 typical shaped particles which is shown in Figure 1(b) together with the RBC. All of these particles have the same volume as the spherical one with diameter 1 μm. In addition to the RBC model, the details of these particles such as the surface area and discretization parameters are listed in Table. 1. A rectangular channel is adopted to represent the blood vessel shown in Figure 1(a). Due to limit of computational resource, only part of the vessel with length of 54 μm (y-direction), width of 27 μm (x-direction) and height of 36 μm (z-direction) is employed. We applied periodic boundary conditions in length and width directions. And height direction is bounded by two fixed flat plates. The flow is driven by pressure difference in y-direction. Then the flow configuration in y-z plane is parabolic (plane Poiseuille flow) whose velocity contour is displayed in Figure 1(a). Because the channel size is not small ($\sim 36\ \mu m$ in height), this slit-like channel can reproduce the similar results compared to those in the tubular channel. Based on the 2D Poiseuille flow, the velocity profile in shear plane (y-z plane) should be $v(z) = -\frac{\bigtriangledown p}{2\mu L} z(h-z)$, where v is the velocity along y-direction, $\bigtriangledown p$ is the pressure difference between the inlet and outlet with distance L in flow direction (y-direction) and h is the height of the channel. The wall shear rate $\dot{\gamma}_\omega$ is defined as: $\dot{\gamma}_\omega = \frac{dv(z)}{dz}|_{z=0} = -\frac{\bigtriangledown p h}{2\mu L}$. In the rest of this work, the shear rate points to wall shear rate unless otherwise stated. 162 RBCs and 80 MPs are randomly placed in the channel. Then the hematocrit in present study is about 29.1%. In the human body's microvasculature network, the hematocrit locates within the range $20 \sim 40\ \%$[26]. Here, we choose an intermediate value. It should be noted that the MPs are initially constrained within the center region of the channel. It on one hand results in the more obvious margination behaviors of MPs, and on the other hand make the comparison of MPs with different shapes more convincing through eliminating the influence of initial configuration. In our mulations, the wall shear rate $\dot{\gamma}_\omega$ is varied by tuning the pressure difference $\bigtriangledown p$. And the dimensionless time in the results is defined as: $t^* = t\dot{\gamma}_\omega$.

2.2 Numerical method

2.2.1 Lattice Boltzmann method for fluid flow

Due to ignorance of minorities of blood components such as protein and glucose, the blood plasma behaves as a Newtonian fluid. The dynamics is governed by the continuity equation and incompressible Navier-Stokes (NS) equation:

$$\nabla \cdot \mathbf{v} = 0, \tag{1}$$

$$\frac{\partial \mathbf{v}}{\partial t} + \mathbf{v} \cdot \nabla \mathbf{v} = -\frac{\nabla p}{\rho} + \mu \nabla^2 \mathbf{v} + \mathbf{F}, \tag{2}$$

where ρ is the plasma density, $\mathbf{v}$ is the velocity of flow, and p represents the pressure of the flow. $\mathbf{F}$ is the body force and μ is the dynamic viscosity of the plasma. We employ the Lattice Boltzmann method (LBM) to solve the NS equation. LBM is one of the fluid dynamics solver with over 20 years development[31]. It is adopted due to its high efficiency and natural parallelism. And it is confirmed that LBM is accurate enough to handle incompressible Newtonian flow. Based on the linearized Boltzmann equation, a finite difference scheme can be obtained by discretizing velocity in Eulerian space:

$$f_i(\mathbf{x} + \mathbf{e}_i \Delta t, t + \Delta t) = f_i(\mathbf{x}, t) - \frac{\Delta t}{\tau}(f_i - f_i^{eq}) + F_i, \tag{3}$$

where $f_i(\mathbf{x}, t)$ is the distribution function and $\mathbf{e}_i$ is the discretized velocity. Current simulations adopt the D3Q19 velocity model, and the details such as the discretized velocity value and direction are introduced in Mackay *et al.*[32]. In the Eq. (3), τ is a non-dimensional relaxation time scale, and it is related to the dynamic viscosity of the fluid with the form: $\mu = \rho c_s^2 (\tau - \frac{1}{2})\Delta t$. $f_i^{eq}(\mathbf{x}, t)$ is the equilibrium distribution function and F_i is the discretized scheme of external force. They have the form[33]:

$$f_i^{eq}(\mathbf{x}, t) = \omega_i \rho \left[1 + \frac{\mathbf{e}_i \cdot \mathbf{u}}{c_s^2} + \frac{(\mathbf{e}_i \cdot \mathbf{u})^2}{2c_s^4} - \frac{(\mathbf{u})^2}{2c_s^2} \right], \tag{4}$$

and

$$F_i = (1 - \frac{1}{2\tau})\omega_i \left[\frac{\mathbf{e}_i - \mathbf{u}}{c_s^2} + \frac{(\mathbf{e}_i \cdot \mathbf{u})}{c_s^4} \mathbf{e}_i \right] \cdot \mathbf{F}, \tag{5}$$

where the weighting coefficients $\omega_i = 1/3\ (i = 0), \omega_i = 1/18\ (i = 1-6), \omega_i = 1/36\ (i = 7-18)$. The term c_s represents the sound speed which equals $\Delta x/(\sqrt{3}\Delta t)$.

Here, the solver of LB we adopt is the embedded form in Large-scale Atomic/Molecular Massively Parallel Simulator (LAMMPS)[34], which is implemented by Mackay *et al.*[32]. The macroscopic properties of the fluid density and velocity can be calculated as the following form after the particle density distributions are known:

$$\rho = \sum_i f_i,\ \mathbf{u} = \frac{1}{\rho} \sum_i f_i \mathbf{e}_i + \frac{1}{2\rho} \mathbf{F} \Delta t. \tag{6}$$

2.2.2 Coarse-grained model for RBCs and MPs

A coarse-grained model is developed to capture the dynamics of RBC, and it is implemented into LAMMPS. Utilizing the high efficiency of LAMMPS due to its optimal parallelization, large scale systems with thousands, even millions of RBCs can be handled. In our simulations, a RBC is modeled as two dimensional liquid-filled coarse-grained membrane with no thickness. It is discretized into 3286 vertices and 6568 triangular elements. We use a series of potential functions to capture the mechanical behaviors of RBC. The stretching potential $U_{stretching}$ is used to describe the in-plane shear property of RBC through coupling attractive nonlinear spring potential - worm-like chain model (WLC) with repulsive power potential - power function (POW)[35,36]:

$$U_{WLC} = \frac{k_B T l_m}{4p} \frac{3x^2 - 2x^3}{1 - x},\ U_{POW} = \frac{k_p}{l}, \tag{7}$$

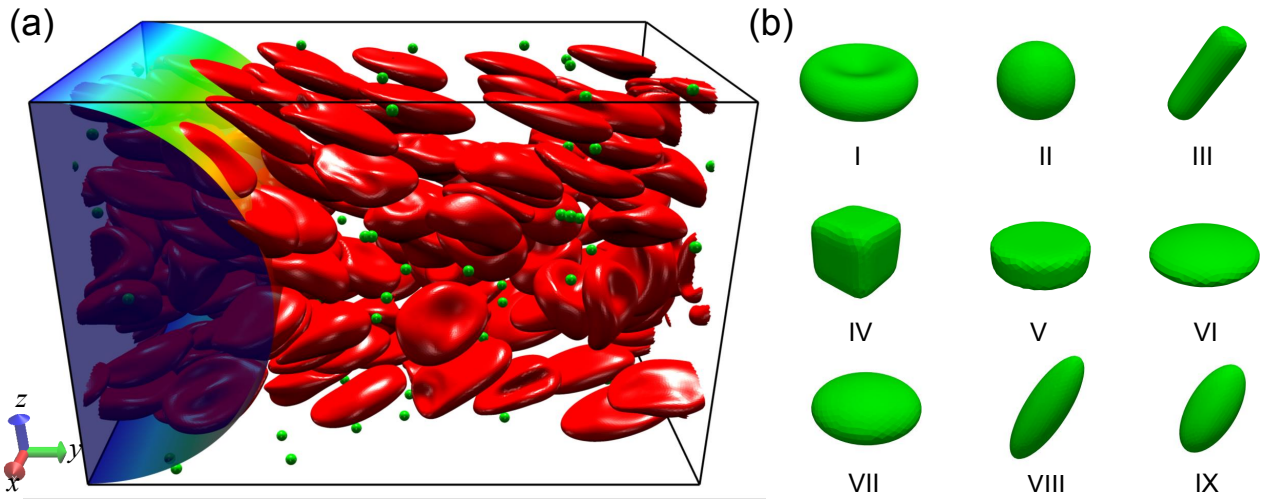

Fig. 1 (a) Computational model of blood flow. (b) Shapes of RBC and 8 different shaped particles.

Domain size: $27\mu m \times 54\mu m \times 36\mu m$

162 RBCs and 80 Particles

Ht = 0.3

$$u(z) = \frac{G}{2\mu} z(h-z) \qquad u_m(z) = \frac{Gh^2}{8\mu}$$

$$\gamma_w = \frac{du(z)}{dz}\Big|_{z=0} = \frac{Gh}{2\mu}$$

Table 1 Parameters of RBC and MPs in simulations.

Type	Volume (μm^3)	Surface area (μm^2)	Vertices	Elements	Surface area to volume ratio (SVR (μm^{-1}))
I. RBC	94.1	134.1	3286	6568	-
II. Sphere	0.52	3.14	198	392	6.0
III. Rod	0.52	3.63	326	648	6.95
IV. Cubic	0.52	3.16	196	368	6.05
V. Disc	0.52	3.66	196	388	7.01
VI. Oblate (AR=3)	0.52	3.93	318	632	7.51
VII. Oblate (AR=2)	0.52	3.43	334	664	6.55
VIII. Prolate (AR=3)	0.52	3.70	318	632	7.07
IX. Prolate (AR=2)	0.52	3.37	342	680	6.45

where $k_B T$ is the energy unit. $x = l/l_m \in (0,1)$, represents the extension ratio, l is the length of the spring and l_m is the maximum spring extension. p is the persistent length, and k_p is the POW force coefficient. The coefficients are calibrated by the physical value of the shear modulus which will be discussed later. The out-of-plane torsion of RBC is reflected by applying potential function:

$$U_{bending} = \sum_{k \in 1 \ldots N_s} k_b [1 - \cos(\theta_k - \theta_0)], \tag{8}$$

where k_b is the stiffness coefficient. θ_k is dihedral angle between two adjacent triangular elements, and θ_0 is the initial value of dihedral angle. In the following, subscript 0 represents the corresponding initial value unless otherwise stated. N_s denotes the total number of dihedral angles. The bulk properties, including surface area and volume conservation, are ensured by introducing the penalty forms:

$$U_{\text{area}} = \sum_{k=1 \ldots N_t} \frac{k_d (A_k - A_{k0})^2}{2A_{k0}} + \frac{k_a (A_t - A_{t0})^2}{2A_t}, \tag{9}$$

and

$$U_{\text{volume}} = \frac{k_v (V - V_0)}{2V_0}, \tag{10}$$

where in Eq. (9), the two terms represent the local area and global area constraint, respectively. A_k and A_t are the area of k-th element and the total membrane, and k_d and k_a are the corresponding spring constants, respectively. In Eq. (10), k_v is the spring constant and V is total volume.

Then the total energy U is:

$$U = U_{WLC} + U_{POW} + U_{bending} + U_{area} + U_{volume}. \tag{11}$$

The nodal forces exerted on vertexes of the membrane are derived by:

$$f_i = -\partial U(X_i)/\partial X_i, \tag{12}$$

where X_i denotes the vertex of membrane. Thus, if we know the position of membrane vertexes, we can calculate the nodal force according to Eq. (12). We choose the parameters in the coarse-grained model of RBC through calibrating the macroscopic properties with following relationship[35,37,38]:

$$\begin{aligned} \mu_0 &= \frac{\sqrt{3}k_B T}{4pl_m x_0}\left(\frac{x_0}{2(1-x_0)^3} - \frac{1}{4(1-x_0)^2} + \frac{1}{4}\right) + \frac{3\sqrt{3}k_p}{4l_0^3}, \\ K &= 2\mu_0 + k_a + k_d, \\ Y &= \frac{4K\mu_0}{K+\mu_0}, \end{aligned} \tag{13}$$

where μ_0 is the shear modulus, K represents the area compression modulus and Y denotes the Young's modulus. Through comparing these macroscopic properties with those in experiments, we can validate the accuracy of our developed model. And this process

has been discussed in our previous works[39,40].

The above model is also applied to approximately model rigid MPs. Because the above potentials describe elastic properties of the membrane, we consider rigid MPs as particles with high stiffness and high stretching coefficient. We enlarge the coefficients involving in the potential functions of RBC by one order except the change of shear modulus is two order higher. Additionally, we impose about 2% volume expansion to the initial state of MPs. The details of the parameters used in the simulations are listed in ESI†Table. S1. In addition to the above potentials, it is necessary to employ inter-molecular potential among RBCs to characterize their interactions. Here we use the Morse potential as inter-molecular interactions[18,36,41]:

$$U_{morse} = D_0[e^{-2\beta(r-r_0)} - 2e^{-\beta(r-r_0)}], r < r_c, \tag{14}$$

where D_0 represents the energy well depth and β controls the width of potential well, r is the distance between two particles and r_0 is the equilibrium distance, r_c is the cutoff distance. Additionally, a short range and pure repulsive Lennard-Jones (LJ) potential is applied to prevent the overlap between RBCs and MPs[40]. It should be noted that the Morse potential and LJ potential are applied on the vertices of RBCs and MPs. The parameters of morse potential and LJ potential are provided in ESI†Table. S1.

2.2.3 Immersed boundary method

The LBM and LAMMPS, which account for fluid and structure dynamics respectively, are coupled by the immersed boundary (IB) method. IB was firstly proposed by Peskin[42] to investigate the heart valve motion in the blood flow. And it is developed to simulate deformable objects immersed in the flow. Detailed derivation and application of IB method can be found in Refs.[43–46]. Briefly, we use the Lagrangian ($\mathbf{X}$) and Eulerian ($\mathbf{x}$) mesh points in the computational domain to represent RBC and fluid particles, respectively. The Eulerian mesh is uniform and the resolution is $\Delta x = 250\ nm$ in all directions. The Lagrangian mesh for RBC or MP is created by MATLAB[47,48]. The mesh is approximately uniform and the size is about $\Delta X = 0.6 \sim 0.8\Delta x$. There are about 32 Eulerian points across major axis of one RBC. This is accurate enough to capture the deformation and motion of RBCs[24,49]. The coupling is fulfilled by the interpolation of velocity and force distributions between Lagrangian and Eulerian mesh points[50].

First, to ensure no-slip boundary condition, the membrane vertices $\mathbf{X}$ with Lagrangian coordinate s should move with the same velocity as the fluid around it. That is:

$$\frac{\partial \mathbf{X}(s,t)}{\partial t} = \mathbf{u}(\mathbf{X}(s,t)). \tag{15}$$

The velocity can be interpolated by the fluid velocity through a smoothed Dirac-Delta function δ:

$$\mathbf{u}(\mathbf{X},t) = \int_\Omega \mathbf{u}(\mathbf{x},t)\delta(\mathbf{x}-\mathbf{x}(\mathbf{X},t))d\Omega. \tag{16}$$

In the present 3D study, four-points interpolation template is adopted, and it is chosen to be:

$$\delta(\mathbf{x}-\mathbf{x}^s(\mathbf{X}^s,t)) = \delta(x-x(\mathbf{X}^s,t))\delta(y-y(\mathbf{X}^s,t))\delta(z-z(\mathbf{X}^s,t)), \tag{17}$$

where

$$\delta(r) = \begin{cases} \frac{1}{4}(1+\cos(\frac{\pi|r|}{2})), & r \le 2 \\ 0. & r > 2 \end{cases} \tag{18}$$

Then the membrane moves with the velocity $\mathbf{u}(\mathbf{X},t)$, and membrane force density $\mathbf{F}(s,t)$ is obtained by derivation of the potential functions mentioned above. We distribute it to the surrounding fluid mesh points by the form:

$$\mathbf{f}^{fsi}(\mathbf{x},t) = \int_\Omega \mathbf{F}^{fsi}(\mathbf{X},t)\delta(\mathbf{x}-\mathbf{x}(\mathbf{X},t))d\Omega. \tag{19}$$

Afterwards, the fluid solver can update with this force density. The above simulation scheme has been discussed in our previous work in detail[40].

3 Results and Discussion

In this part, the quantification of margination probability is firstly defined. Secondly, we adopt the sphere MP as an example to illustrate the dependence of margination behavior of MPs on wall share rate. Lastly, we vary the shape of MPs and compare their margination behaviors under different wall shear rates.

3.1 Quantification of margination probability

Apart from the definition, to have a direct observation, we show the snapshots for margination behavior in Figure 2. At initial state $t^* = 0$, RBCs are in rest biconcave shapes and MPs are placed among RBCs, but constrained around the center of channel. As simulation progresses, at $t^* = 800$, the whole system displays parabolic shape due to the Poiseuille flow pattern. The biconcave shape of RBC vanishes and RBCs align their major axes along the shear direction. The most obvious phenomenon is that MPs accumulate near the vessel wall. And this is more significant when the simulation time further increases to $t^* = 2500$.

Before quantifying the margination behavior of MPs, the thickness of CFL should be estimated. Firstly, we remove MPs and only leave RBCs in the channel. We apply different wall shear rates and calculate the thickness of CFL using the same method proposed by Fedosov *et al.*[51]. Figure 3(b) gives the result for CFL thicknesses under different wall shear rates $\dot{\gamma}_\omega$ from 200 s^{-1} to 2000 s^{-1}. We find that the CFL thickness increases with the increment of $\dot{\gamma}_\omega$ when $\dot{\gamma}_\omega < 1000$. Further increase of $\dot{\gamma}_\omega$ results in approximately constant, even small decrease of the CFL thickness. This is consistent with the previous experimental and computational results[51–53] shown in the Figure. The increase of CFL thickness is attributed to the deformation of RBCs. When $\dot{\gamma}_\omega$ increases, the deformation of RBC becomes more significant, and the lift force RBC experienced due to the existence of vessel wall increases[54–56]. However, higher shear rate can also strengthen the hydrodynamic interactions among RBCs, which tend to expand RBC core in the flow. Thus, further increase of shear rate could lead to small decrease of the CFL thickness.

Knowing the CFL thickness, we can investigate the margination behavior of MPs quantitatively. We use the margination probability $\Pi(t)$ to characterize it. $\Pi(t)$ is defined as:

$$\Pi(t) = \frac{n_f(t) - n_f(0)}{N}, \tag{20}$$

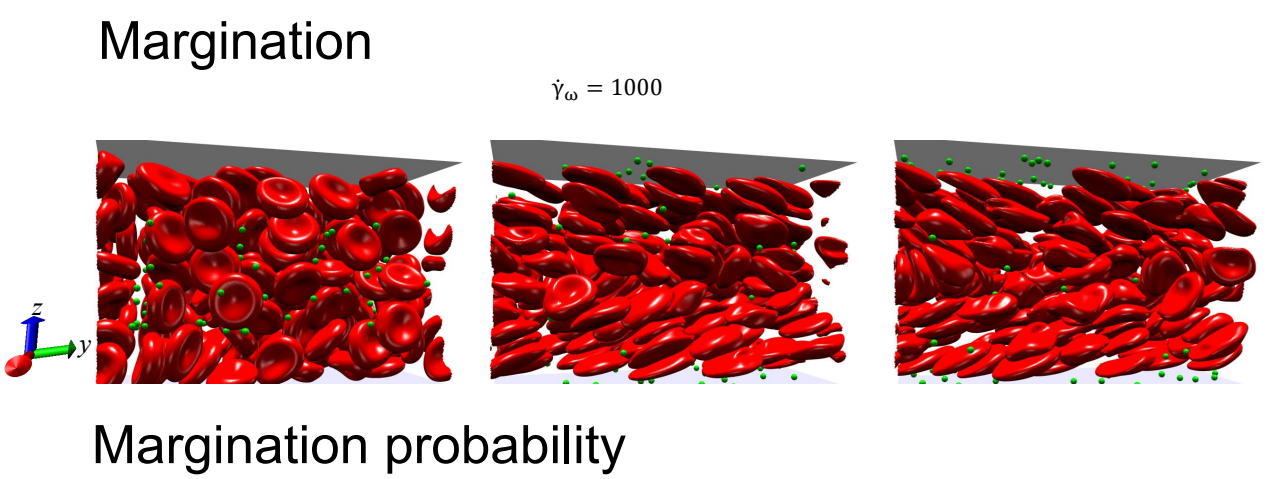

Fig. 2

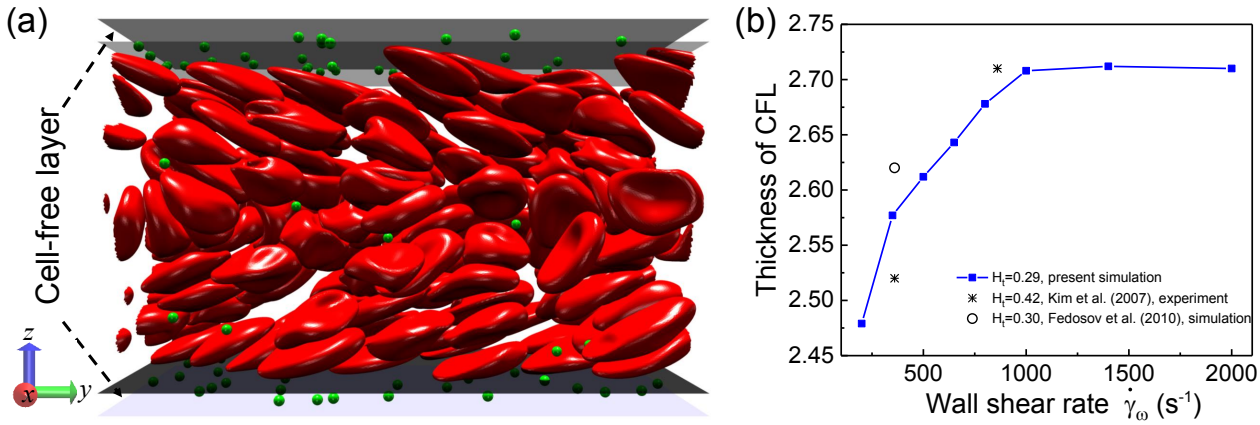

Fig. 3 Calculation of the CFL thickness. (a) Schematic of CFL in the blood flow. Shaded planes represent the boundaries of CFL. (b) Thickness of the CFL under different wall shear rates.

$$\Pi - \frac{N_{CFL}(t)}{N}$$

where $n_f(t)$ represents the number of MPs with centers locating within the CFL at time t, and N denotes the total number of MPs in the channel. Note that we constrain MPs within the center region at the beginning of simulation $n_f(0) = 0$. In Figure 3(a), the boundaries of CFL are illustrated as the shaded planes. When the center of MP enters the region between CFL boundary and vessel wall, we count it as marginated MP.

Figure 4(a) shows the evolution of the margination probability for sphere MP under wall shear rate 500 s^{-1} and 1000 s^{-1}. We find that the evolution of margination probability can be split into three stages. At first stage ($t^* < 500$), the margination probability dramatically increases as the simulation advances. After that, in the second stage ($500 < t^* < 1800$), the growth rate of margination probability slows but still increases with further increase of simulation time. At the last stage ($t^* > 1800$), it mostly reaches a plateau with small variations. At the same time, we find the margination probability fluctuates with the time. In some time intervals, the fluctuations are significant. So when we take the averaged value of the margination probability, the choice of the averaged time interval should be very important. Here, there are two steps for calculating the averaged value of margination probability. The first step is varying the integration time interval and then we can obtain the evolution of the averaged margination probability. The formulation is:

$$\langle \Pi \rangle = \frac{1}{T} \int_{t_{total}-T}^{t_{total}} \Pi(t) dt, \tag{21}$$

where t_{total} is the total simulation time, and T is the integration backward time interval from the end of simulation. The evolution of averaged margination probability against T is shown in Figure 4(b). We find that when T is small ($T < 250$), the averaged values of margination probability are significant different. It manifests that the averaged value of margination probability strongly depends on the choice of T. However, $\langle \Pi \rangle$ becomes approximately constant with small fluctuation with further increase of T. After we obtain the evolution of $\langle \Pi \rangle$, the second step is to calculate the distribution of $\langle \Pi \rangle$. For example, for the sphere MP under $\dot{\gamma}_\omega = 500\ s^{-1}$, the minimum value of $\langle \Pi \rangle$ in Figure 4(b) is about 0.675, and the maximum value is about 0.752. Then we split this regime into several bins with size 0.005. We count the value of $\langle \Pi \rangle$ locating within these bins and calculate their distributions as shown in Figure 4(c). From these distributions, it is obvious that the value 0.68 is the most possible $\langle \Pi \rangle$, and we take it as the ultimate $\langle \Pi \rangle$. If the distribution of two adjacent bins are close like the case of sphere MP under $\dot{\gamma}_\omega = 1000\ s^{-1}$ shown in Figure 4(d), we take the averaged value of these two bins as the ultimate $\langle \Pi \rangle$. More cases are given in the ESI†Fig. S1.

3.2 Shear rate dependent margination

For simplicity, we adopt sphere MP as a typical case to demonstrate the shear rate dependent margination of MPs. Figure 5 presents the particle concentration along height direction (z-direction) of the channel. The height direction is split into bins

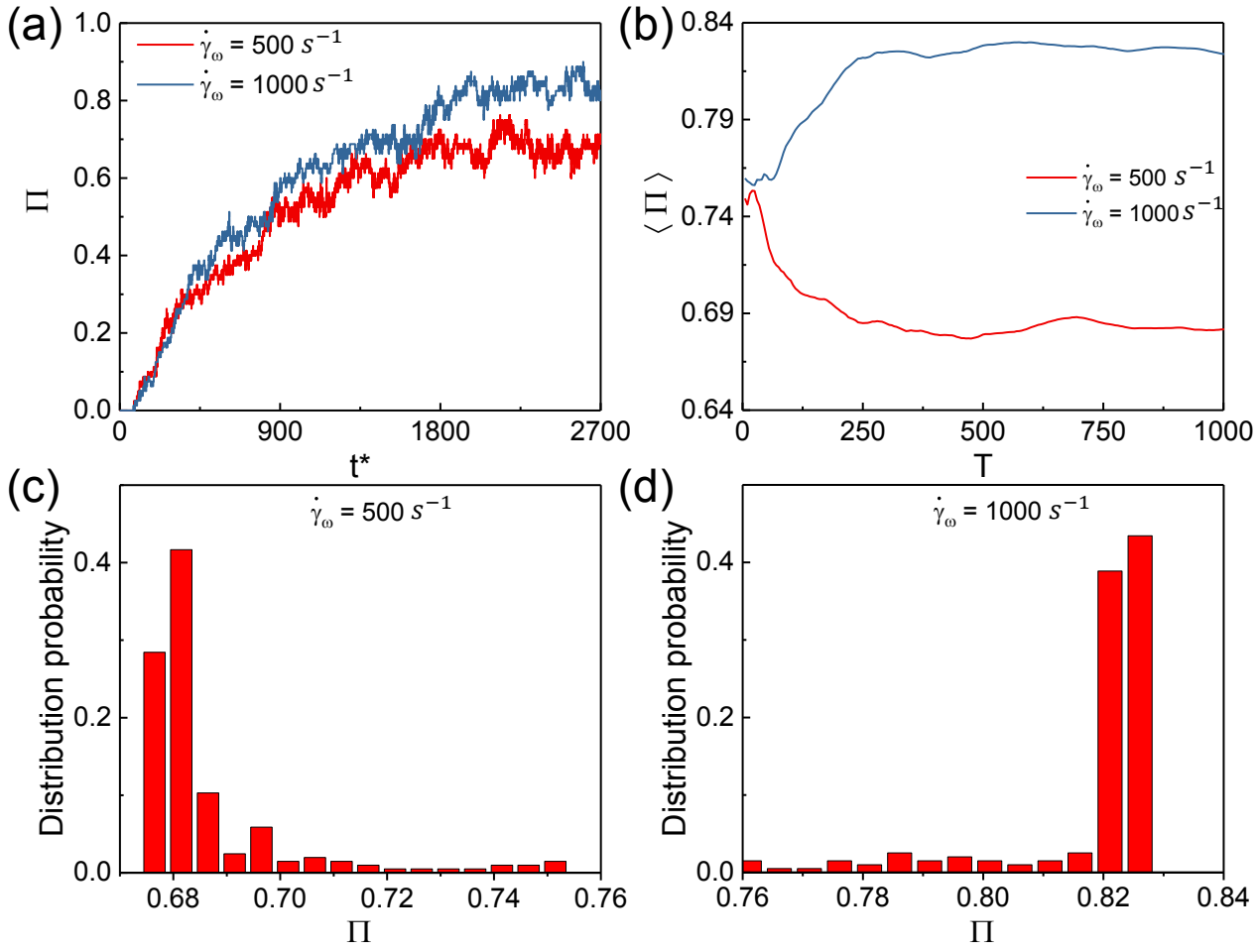

Fig. 4 Calculation of the margination probability for sphere MP under wall shear rate $500\ s^{-1}$ and $1000\ s^{-1}$. (a) Evolution of the margination probability. (b) Relationship between the averaged margination probability and the integration interval. (c) and (d) are the distribution of the averaged probability.

with the same size 3 μm, which is comparable to the CFL thickness. Then the particle concentration in the bins near the vessel wall can reflect accumulation of MPs in the CFL. We compare the particle concentration of sphere MP under $\dot{\gamma}_\omega = 200\ s^{-1}$ and $\dot{\gamma}_\omega = 500\ s^{-1}$. The initial state ($t^* = 0$) of them are the same, but when simulation progresses, the particle concentration near the wall under high shear rate ($\dot{\gamma}_\omega = 500\ s^{-1}$) is more than that under low shear rate ($\dot{\gamma}_\omega = 200\ s^{-1}$). And the particle concentration differences between these two cases are more significant at the end of these simulations. This phenomenon shows that the increment of shear rate can promote the margination behavior of sphere MPs.

To quantify the margination behavior under different shear rates, we calculate the averaged margination probability according to the method mentioned above. Figure 6(a) shows the relationship between the averaged margination probability $\langle\Pi\rangle$ and shear rate $\dot{\gamma}_\omega$. It is found that $\langle\Pi\rangle$ increases with the increment of shear rate, but the relationship is not simple. When shear rate is low ($\dot{\gamma}_\omega < 800\ s^{-1}$), $\langle\Pi\rangle$ increases dramatically, while under higher shear rate the growth rate of $\langle\Pi\rangle$ becomes smaller. There is almost no difference between the cases with $\dot{\gamma}_\omega = 800\ s^{-1}$ and $\dot{\gamma}_\omega = 1000\ s^{-1}$.

The mean-squared displacement (MSD) of MPs is firstly examined to understand the underlying mechanism dominating the shear rate dependent margination shown in Figure 6(a). Figure 6(b) presents the MSD result of sphere MPs in the flow under different shear rates. In blood flow, the deformation of RBCs induces the velocity fluctuation of the flow around them. This perturbated flow causes the migration of particles either to center region of channel or towards the vessel wall in the blood flow[57]. From Figure 6(b), we find that the MSD of MPs splits into two stages. The diffusion of MPs in the first stage is stronger than that in the second stage. We calculate the diffusivity defined as $D =< \Delta z^2 > /2t$ in the first stage to account for the diffusional cross-flow motion of MPs. It is found that D ranges from about 4 to $5 \times 10^{-8} cm^2 s^{-1}$. The results are consistent with previous studies[24,58]. It should be noted that this diffusivity is about 20 times larger than that in Brownian motion. According to Stokes-Einstein Equation: $D = \frac{k_B T}{6\pi\mu r}$, where k_B is the Boltzmann constant, T is temperature, μ is the dynamic viscosity of fluid and r is the radius of the particle, we assume the T is the human body temperature 37 $^\circ C$, and μ is the corresponding plasma viscosity 1.2 cp, r is about 0.5 μm, the diffusivity is about $1.8 \times 10^{-9} cm^2 s^{-1}$. We further examine whether this is induced by the existence of RBCs or not. We remove the RBCs in the flow, and monitor the migration of MPs under the same flow condition. We find that the diffusion

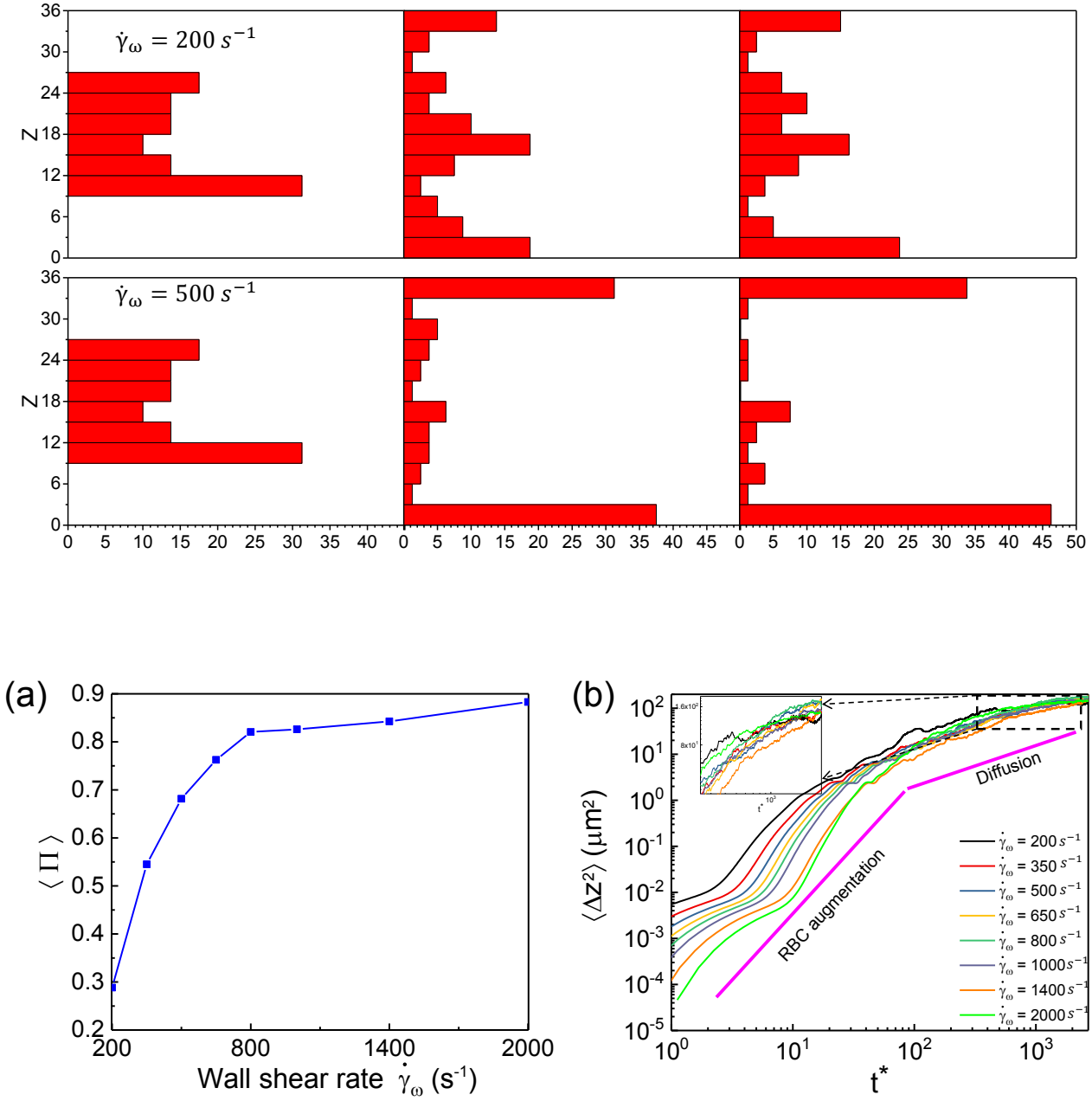

Fig. 6 (a) Averaged margination probability $\langle \Pi \rangle$ against the wall shear rate $\dot{\gamma}_\omega$. (b) Mean-squared displacement $< \Delta z^2 >$ of sphere MPs in the blood flow under different shear rates.

is very weak. We estimate the diffusivity $D = 3.8 \times 10^{-9} cm^2 s^{-1}$. It's about 10 times smaller than that with RBCs in the flow, which means RBCs in the blood flow promote the diffusion of particles. We should also note that current simulations cannot consider the hydrodynamic fluctuations due to limitation of computational method. There exists small, but significant differences among the diffusions of MPs under different wall shear rates. The diffusivity increases with the increment of the wall shear rate. Here diffusivity is an indication of the interaction between RBCs and particles. The difference for the shear rate dependent diffusion of MPs should be attributed to the interaction between RBCs and particles. This will be discussed in detail later.

Since the flow approximates Stokes flow, the inertial effect is negligible here. The cross-flow motion of sphere MPs should be independent on the shear rate due to the symmetry of Stokes flow. Thus, the shear rate dependent margination of MPs should rely on the existence of RBCs.To confirm this hypothesis, we conduct simulations to monitor the margination of sphere MPs without RBCs in the channel. We find that the margination of MPs is very small compared to that with RBCs in the flow (see ESI†for details). We inspect structures of RBCs in the blood flow under different shear rates in Figure 7. When shear rate is not high ($\dot{\gamma}_\omega < 500\ s^{-1}$), the rouleaux structure induced by the aggregation of RBCs is obvious in the blood flow, and it is denoted by using the dashed blue circle. The aggregation of RBCs is caused by the discoid shape and interaction between RBCs[41,59,60]. As the structure of aggrega-

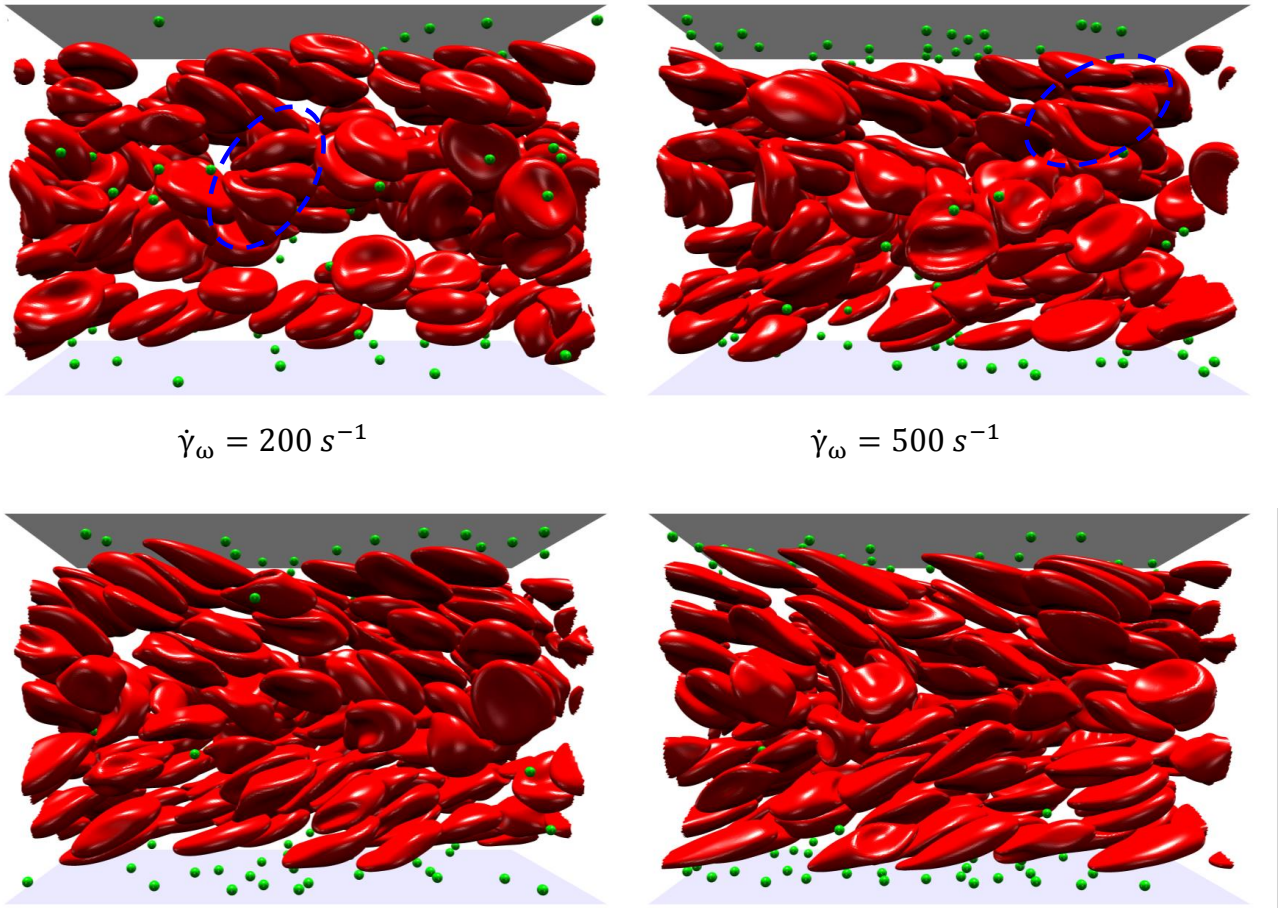

Fig. 7

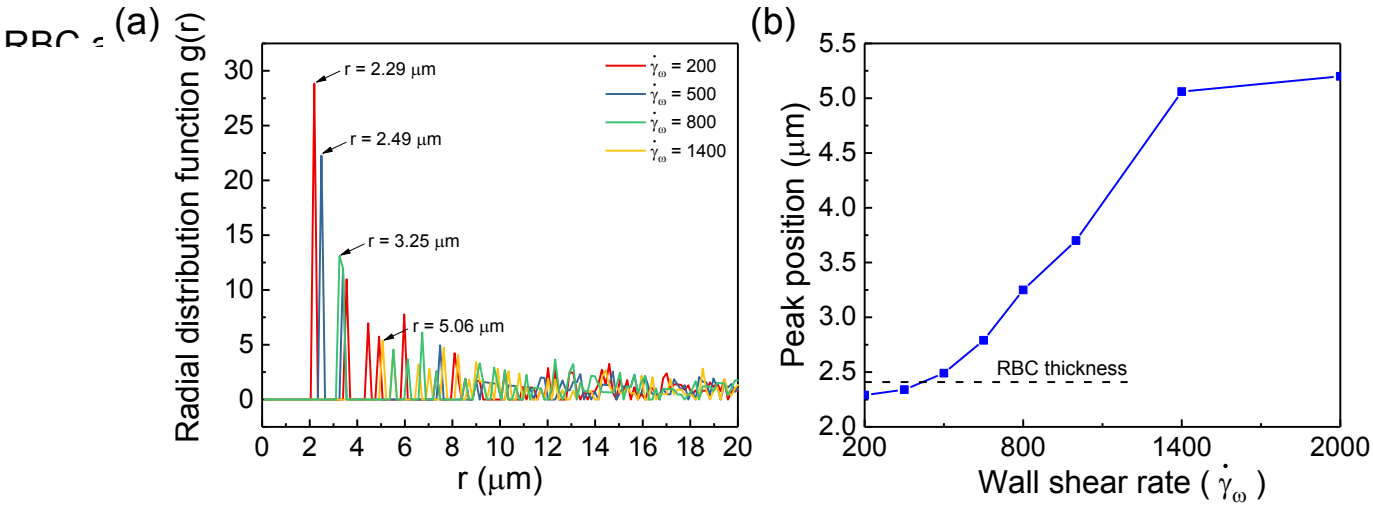

Fig. 8 (a) Center-of-mass radial distribution function $g(r)$ of RBCs under different shear rates. (B) First peak location of $g(r)$ for RBCs under different shear rates.

tion is rouleaux-like, the center distance between two RBCs in the structure is about the same as the thickness of RBC ($\sim 2.33\ \mu m$). We examine the center-of-mass radial distribution function $g(r)$ of RBCs under different shear rates and show the results in Figure 8. In Figure 8(a), when $\dot{\gamma}_\omega < 800\ s^{-1}$, the first peaks of $g(r)$ approximate the thickness of RBC. While after $\dot{\gamma}_\omega >= 800\ s^{-1}$, the peaks shift to larger values, which means the rouleaux structure is not significant and even vanishes. Figure 8(b) presents the

first peak positions for RBCs under different $\dot{\gamma}_\omega$, we can find that peak position increases with the increment of $\dot{\gamma}_\omega$. Additionally, from Figure 8(a), as the $\dot{\gamma}_\omega$ increases, the value of $g(r)$ decreases, meaning the RBC aggregations in the flow gradually reduce. When the rouleaux forms, there are more void space between their aggregates in the blood flow as the hematocrit is constant. This phenomenon is more obvious when the shear rate is low ($\dot{\gamma}_\omega = 200\ s^{-1}$). However, the rouleaux structure vanishes when the shear rate is higher ($\dot{\gamma}_\omega = 1000\ s^{-1}$ and $2000\ s^{-1}$). And the distribution of RBCs are more uniform in the blood flow. No significant difference of the RBC structures is found between the cases of $\dot{\gamma}_\omega = 1000\ s^{-1}$ and $\dot{\gamma}_\omega = 2000\ s^{-1}$.

The structure of RBCs should influence the interaction between RBCs and MPs. Hydrodynamic interaction between RBCs and MPs is also named hydrodynamic collision[56,61,62]. Generally speaking, one MP is surrounded by multiple RBCs, and three-body and multi-body effects exist. These effects can only be neglected when the hematocrit is not high ($< 20\%$)[63–65]. In present work, the hematocrit is about 29.1%, the three-body and multi-body effects should play roles in the diffusion of MPs. Although the collision details are difficult to isolate in blood flow, diffusion of MPs is one of indication. From Figure 6(b), the diffusion rate of MPs in blood flow is indeed higher than that in Brownian motion. Hence, hydrodynamic collision augments the diffusion of MPs. However, as mentioned above, the difference of diffusion rates among these cases under different shear rates are not significant. This can not solely reflect the shear rate dependent margination of MPs. Based on the previous study that the near-wall dynamics of platelets is mainly affected by the rebounding collisions with RBCs[20], we believe the hydrodynamic collision between MPs and RBCs in the near-wall region is crucial. Since there is no RBC inside the CFL, the hydrodynamic collision is restricted to pair collision. Vahidkhah *et al.*[24] stated that there are two factors to influence the margination of MP: (i) collision frequency between MP and RBC, and (ii) collision displacement from each individual collision. Here, we also examine these two factors. Figure 9(a) gives some typical trajectories of MPs in the height direction of the channel. It is found that MPs move with the bulk flow at the beginning. Then they may abruptly marginate from the RBC-rich layer to CFL. This phenomenon is named "waterfall" phenomenon[24]. Once MPs enter the CFL, their trajectories are parallel to the wall but with fluctuations (c.f. inserted zoom-in figure in Figure 9(a)). The fluctuation is led by the collisions between MPs and RBCs. The MPs in the edge of CFL region approximately experience the same collision motions with those locating within CFL, because only pair collision happens for those two cases. Then we use the trajectory of MP within CFL to calculate the collision frequency. As shown in the insert of Figure 9(a), the power spectral density analysis is employed to estimate the collision frequency. The result is provided in Figure 9(b). Under different shear rates, we find that the collision frequency increases with the increment of shear rate. It should be noted that the magnitude of collision frequency has the same order of that given in Vahidkhah *et al.*'s work[24], which confirms that this approximation is reasonable. The dependency of collision frequency on shear rate is attributed to the structure of RBCs in the blood flow. When the shear rate is low, the RBCs aggregate together, and form the rouleaux. Void space exists not only in the center of channel, but also in the edge of CFL. Thus, the collision frequency is small. While for the blood flow under high shear rate, the distribution of RBCs along edge of CFL is rather uniform, hence the collision between MPs and RBCs is more frequent.

The pair collision between a single RBC and a single MP is further investigated. The collision model is displayed in Figure 9(c). Because the shear gradient of near-wall flow is almost zero, we use the simple shear flow to represent it. The positions of RBC and MP are set as the same as those in the blood flow. RBC is placed in the RBC-rich layer and MP is in the edge of CFL. The center distance between them is set to be $\sigma = 1\ \mu m$ along height direction and 10σ along flow direction. Here, we also show the collision model of MPs with different shapes. The major axis is placed along the flow direction and other parameters are the same as the sphere MP. After the shear flow is applied, we obtain the collision displacements along the height direction. They are shown in the Figure 9(d) for the sphere MP under different shear rates. Because the size of RBC is much larger (about 8 times) than MP, its collision displacement is negligible compared to the MP. The trajectories of MPs under different shear rates have the same trend. The first approaching between RBC and MP makes the MP abruptly migrate towards the wall. After collision ends, it can partially restore towards its initial position. It locates in a specific equilibrium place between the initial and maximum migration positions. We denote the distance between this equilibrium position and initial position as the collision displacement, which is based on the definition in Refs.[56,61,63]. From the Figure 9(d), we find that the collision displacement is monotonic to the shear rate. It increases with the increment of shear rate.

Combining these two factors: collision frequency and collision displacement of each individual collision, it is clear that under low shear rate, the collision frequency is the lowest and the collision displacement is the smallest. Therefore, the margination probability should be the lowest. Under high shear rate, the collision frequency is high, and the collision displacement is large, so the margination probability is high. Recalling the margination results in Figure 6(a), we find it has the same trend as the collision frequency result. And the relationship between collision displacement and shear rate is almost monotonic. Therefore, we believe the margination of sphere MP is dominated by the collision frequency between MP and RBC. We plot the relationship between collision frequency and margination probability of sphere MP under different shear rates in ESI†Fig. S3. They have the approximately linear relationship. This also explains why the structure of RBCs is responsible for the shear rate dependent margination of MPs.

3.3 Shape effect of MPs on their margination behavior

3.3.1 Comparison of MP margination with different shapes

To investigate the shape effect of MPs on their margination behaviors, 8 different shapes listed in Figure 1(b) are examined under different shear rates. We take two typical shear rates $\dot{\gamma}_\omega = 350\ s^{-1}$ (low) and $\dot{\gamma}_\omega = 1400\ s^{-1}$ (high). The averaged margination prob-

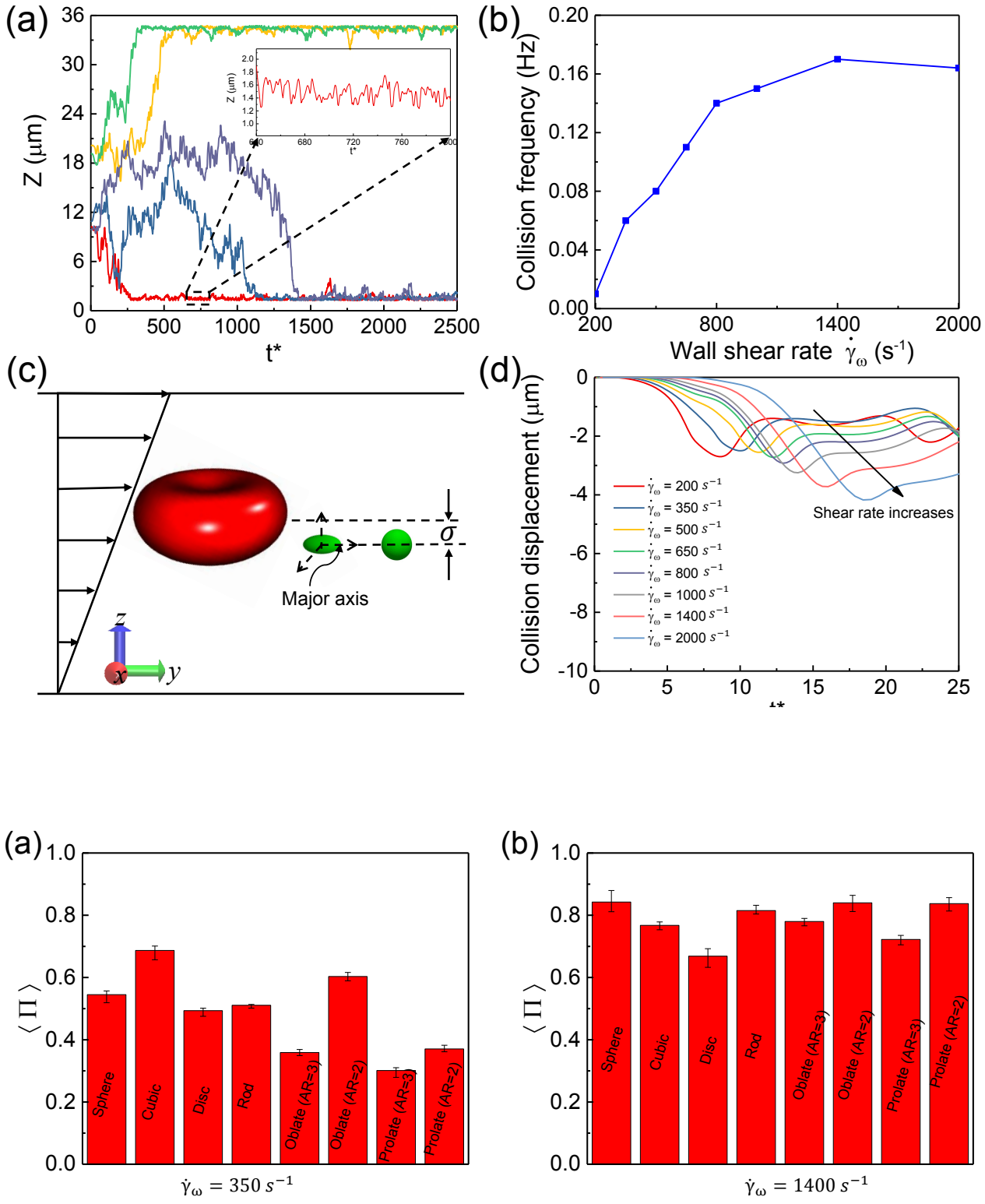

Fig. 10 Comparison of margination probability of different shaped MPs under shear rate (a) $\dot{\gamma}_\omega = 350 s^{-1}$ and (b) $\dot{\gamma}_\omega = 1400 s^{-1}$.

abilities of these MPs are shown in Figure 10. We find when the shear rate is low ($\dot{\gamma}_\omega = 350\ s^{-1}$), the cubic MP demonstrates the strongest margination behavior, followed by the oblate MP with aspect ratio $AR = 2$. The sphere, disc and rod MPs are closely behind. And we find the prolate MP performs the worst as well as oblate MP with aspect ratio $AR = 3$. When the shear rate increases, it is found that the margination probabilities of all different shaped particles increase, but with different amplifications. And the difference of margination probabilities among different shaped particles are not significant compared to that under low

shear rate. The sphere, rod, oblate with $AR = 2$ and prolate with $AR = 2$ are the best and almost the same. What followed are cubic, oblate with $AR = 3$ and prolate with $AR = 3$. The disc particle shows the worst margination. From the direct comparison, another finding is that as for the ellipsoidal particles, including oblate and prolate, particles with low aspect ratio outperform those with high aspect ratio for both of the two shear rates.

Then we vary the shear rate of blood flow to exploit more details of the shape dependency under different shear rates. To make a good comparison, we split these MPs into 3 classes based on their configuration similarity. They are sphere-like, oblate-like and prolate-like MPs. Sphere-like MPs include sphere and cubic; Oblate-like MPs contain disc and oblate; and prolate-like have rod and prolate. It should be noted that the aspect ratio of disc and rod particles are also $AR = 3$. The performance of these MPs under different shear rates are presented in Figure 11(a), (b) and (c). As for the sphere-like particles (c.f. Figure 11(a)), when $\dot{\gamma}_\omega < 800\ s^{-1}$, the cubic is better than sphere, while further increase of shear rate results in stronger margination of sphere than that of cubic. This means there exists a critical shear rate making sphere and cubic demonstrate the same margination. Under this critical value, the cubic is better, and above it, the sphere outperforms cubic. It is also true for the oblate-like particles (c.f. Figure 11(b)). When the shear rate is no more than $800\ s^{-1}$, the disc performs better than oblate ($AR = 3$). And further increase of shear rate makes the oblate ($AR = 3$) outperform the disc. However, although there is also a critical shear rate in which the margination probabilities of rod and prolate ($AR = 3$) are the same, the rod always performs better than the prolate ($AR = 3$) (c.f. Figure 11(c)). Then we choose one case from each of these three classes to make a comparison in the Figure 11(d). It is found that the sphere-like particle performs the best, and there is no obvious trend for the difference of margination between the oblate-like and prolate-like particles.

Further comparison is conducted for the ellipsoidal particles with different aspect ratios. Figure 12 shows the comparison of margination behaviors of ellipsoidal particles with different aspect ratios, including oblate and prolate MPs. In the Figure 12(a), the margination probability of oblate with low AR is always higher than that with high AR. And it is also true for the prolate particles. These two comparisons indicate that the lower the aspect ratio, the higher the margination probability. Considering the shape configuration, it reveals that the more it is close to sphere, the higher the margination probability will be.

3.3.2 Physical mechanism of MP margination in blood flow

To gain a better insight into the above results, we also calculate the individual collision displacements of different shaped MPs and their collision frequencies with RBCs. Here, for simplicity, we also choose the two typical cases: $\dot{\gamma}_\omega = 350\ s^{-1}$ and $\dot{\gamma}_\omega = 1400\ s^{-1}$. They are shown in the Figure 13. When $\dot{\gamma}_\omega = 350\ s^{-1}$, it is found that the prolate-like particles demonstrate the largest individual collision displacement, oblate-like particles follow and the sphere-particles perform the worst. As for the collision frequency, we find that sphere-like particles are the highest, the prolate-like particles are close behind and oblate-like particles are the lowest. Furthermore, we find that under high shear rate $\dot{\gamma}_\omega = 1400\ s^{-1}$, the collision displacement and collision frequency have the same trend compared to those under low shear rate $\dot{\gamma}_\omega = 350\ s^{-1}$. It means that the shape dependent margination of MPs is shear rate independent when only considering the hydrodynamic collision. This can not explain the phenomena we discuss above. For example, for the sphere-like particles: sphere and cubic, the collision displacement and collision frequency of sphere are smaller than those of cubic. Thus, the margination probabilities of sphere under $\dot{\gamma}_\omega = 350\ s^{-1}$ and $\dot{\gamma}_\omega = 1400\ s^{-1}$ should be both lower than those of cubic. However, Figure 11(a) shows that under high shear rate, the sphere outperforms the cubic. From this perspective, the shape dependency should be relevant to the shear rate. Under this circumstance, other factors affecting the margination behavior of MPs should be considered.

Because margination describes the near wall accumulation of MPs, the near wall dynamics of MPs should play a crucial role. When only considering the sphere MP, since the flow is nearly Stokes flow, there is no net transverse migration of rigid sphere when moving near the vessel wall. But the near wall dynamics of non-spherical particles is dependent on the shear rate due to the asymmetry of the flow around MPs[15].

Here the near wall dynamics of MPs with different shapes are investigated. Figure 14(a) shows the simplified near wall dynamics model. We place the MP near the wall with major axis parallel to the wall and with minimum distance 5 μm away from the wall. Also, we apply the simple shear flow. We track the center trajectories of different shaped MPs under $\dot{\gamma}_\omega = 350\ s^{-1}$ and $\dot{\gamma}_\omega = 1400\ s^{-1}$ in Figure 14(b) and (c), respectively. From these trajectories, we find that MPs tumble in the flow, but with different tumbling frequencies. Specifically, MPs are split into two classes: one moves towards the wall and the other migrates away from the wall. For example, under low shear rate ($\dot{\gamma}_\omega = 350\ s^{-1}$), the cubic, oblate ($AR = 2$) and prolate ($AR = 2$) move towards the wall, while the rod, disc, prolate ($AR = 3$) and oblate ($AR = 3$) gradually migrate away from the wall. When increasing the shear rate of the flow ($\dot{\gamma}_\omega = 1400\ s^{-1}$), we find MPs are still split into two classes as the same as that under low shear rate. Only the cubic changes to migrate away from the wall.

To make a direct comparison of the migration displacement of MPs, we take the averaged value over the last 50 dimensionless time intervals. We provide the results in Figure 15. Noted that we put the case of sphere MP in the figures as comparison. The migration displacement is zero with no dependence on the shear rate of flow as discussed above. In these figures, positive value means moving towards the wall and negative value denotes the migration away from the wall. Under low shear rate ($\dot{\gamma}_\omega = 350\ s^{-1}$), the migration away from the wall of rod MP is significant and followed by disc, oblate ($AR = 3$) and prolate ($AR = 3$). The moving towards the wall of cubic, oblate ($AR = 2$) and prolate ($AR = 2$) are comparative. When the shear rate is high ($\dot{\gamma}_\omega = 1400\ s^{-1}$), the migration away from the wall of disc becomes stronger, while rod, oblate ($AR = 3$) and prolate ($AR = 3$) have no obvious change compared to those under low shear rate. The moving towards the wall of oblate ($AR = 2$) and prolate ($AR = 2$) decreases. Note that the cubic starts to migrate away

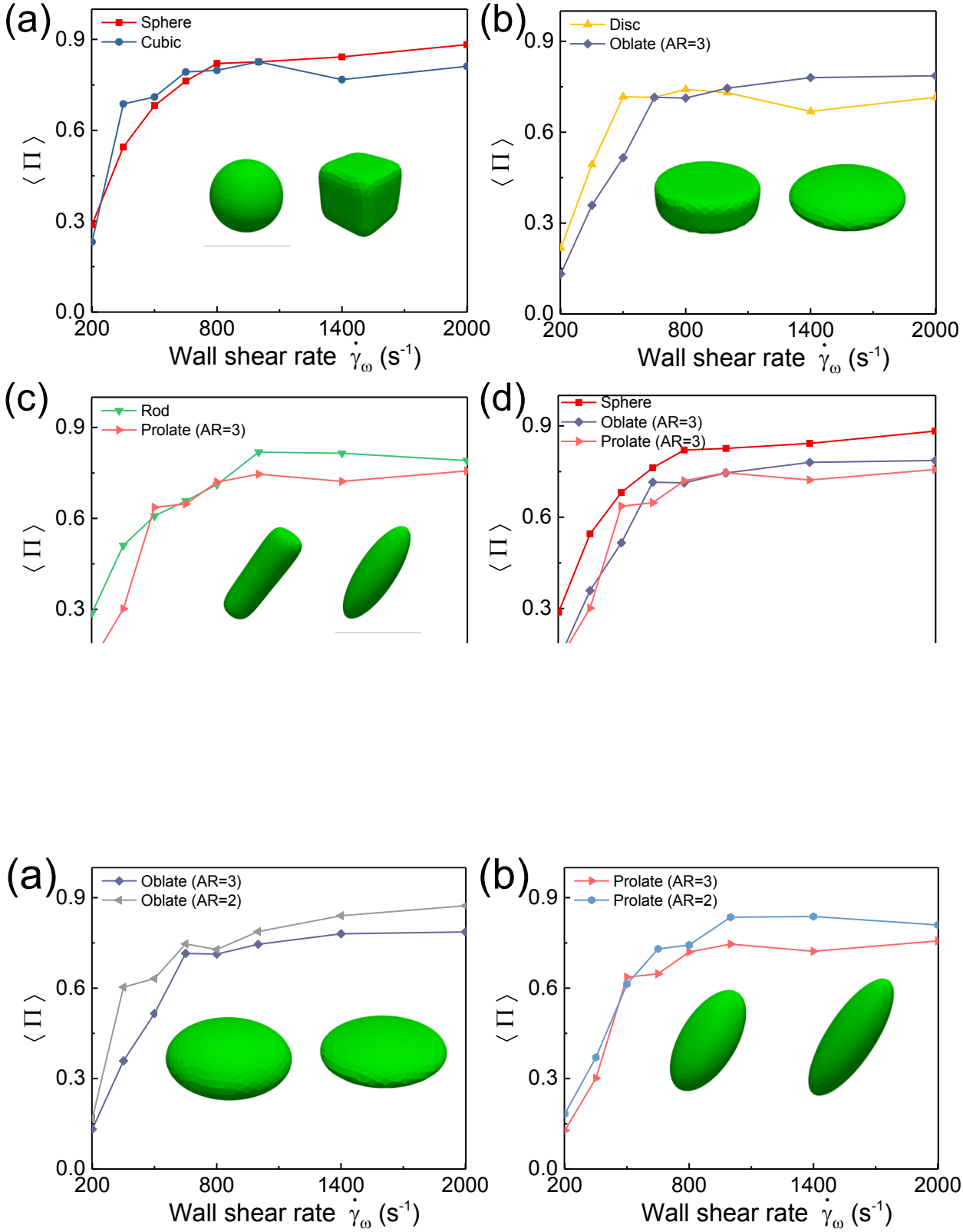

Fig. 12 Comparison of margination probability of MPs with same shape of (a) oblate and (b) prolate, but different aspect ratios ($AR = 2$ and 3).

from the wall under high shear rate, comparing with that moving towards the wall under the low shear rate.

Together with the near wall dynamics of MPs, we use the collision frequency and collision displacement results in Figure 13 to further discuss margination behaviors shown in Figure 11 and Figure 12.

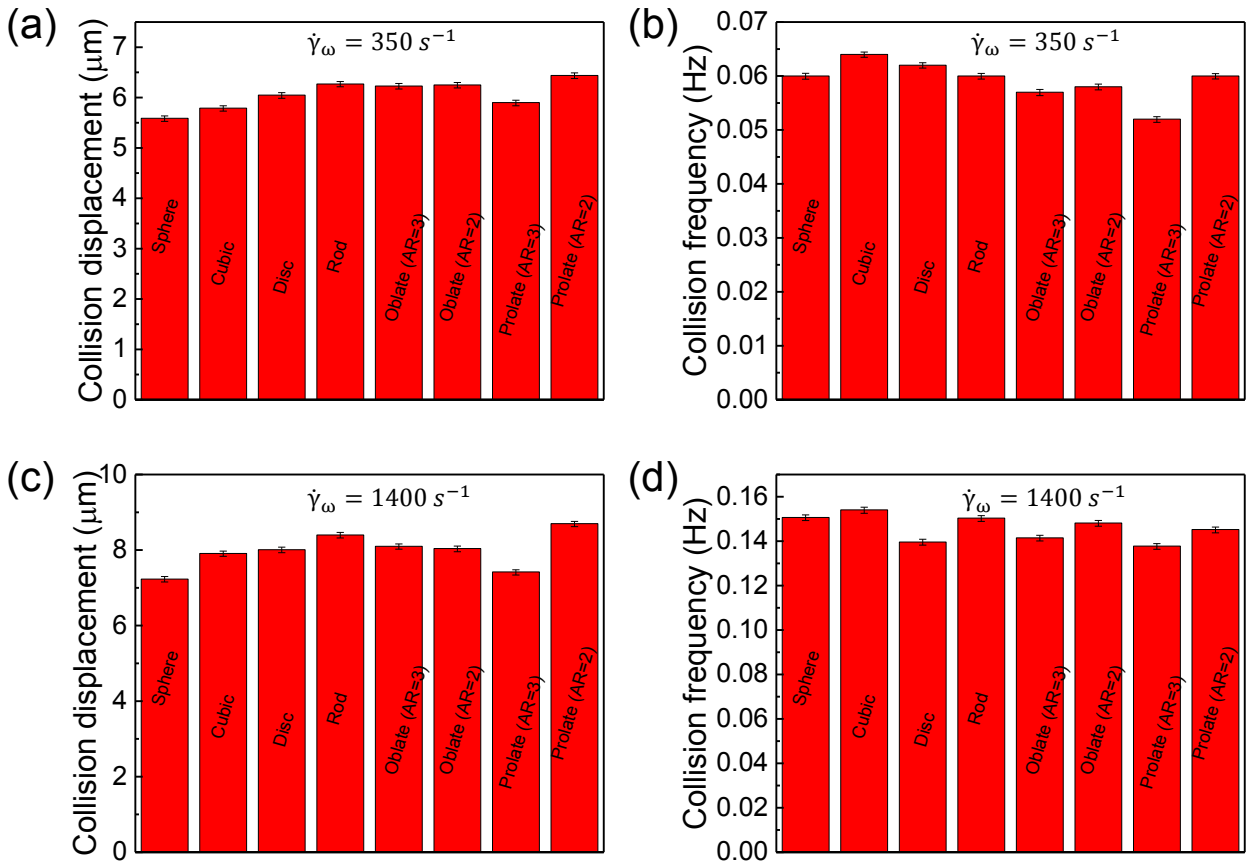

Fig. 13 Hydrodynamic collision between different shaped MPs and RBCs. (a) Collision displacement of individual collision and (b) collision frequency under $\dot{\gamma}_\omega = 350\ s^{-1}$. (c) and (d) are corresponding collision displacement and collision frequency respectively under $\dot{\gamma}_\omega = 1400\ s^{-1}$.

- Sphere-like: Under low shear rate ($\dot{\gamma}_\omega = 350\ s^{-1}$), the collision displacement and collision frequency of sphere are both smaller than those of cubic. Furthermore, sphere has no transverse migration near wall, while the cubic moves towards the wall. Hence, the margination probability of cubic is higher than that of sphere. Under high shear rate ($\dot{\gamma}_\omega = 1400\ s^{-1}$), though the cubic still outperforms sphere on the collision displacement and collision frequency, it has a large migration displacement away from the wall when considering the near wall dynamics. Then, the margination probability of sphere starts to exceed that of cubic.

- Oblate-like: when the shear rate is low ($\dot{\gamma}_\omega = 350\ s^{-1}$), though the collision displacement of disc is smaller than that of oblate ($AR = 3$), the disc outperforms the oblate ($AR = 3$) on the collision frequency. Together with near wall dynamics results that disc migrates away from the wall more than oblate ($AR = 3$), thus, the disc outperforms the oblate ($AR = 3$) on the margination. When the shear rate is high ($\dot{\gamma}_\omega = 1400\ s^{-1}$), both of collision displacement and collision frequency of disc are smaller than that of the oblate ($AR = 3$). Additionally, the migration displacement away from the wall for the disc is significant compared to that of oblate ($AR = 3$). Hence, the oblate ($AR = 3$) demonstrates higher margination probability than that of disc under high shear rate.

- Prolate-like: we can see that both of the collision displacement and frequency of rod are higher than those of prolate ($AR = 3$) under low and high shear rates. In addition, though the rod demonstrates larger migration displacement away from the wall than that of prolate ($AR = 3$), the migration displacement of both are independent on the shear rate. Hence, the rod always performs better than prolate ($AR = 3$).

- Ellipsoid with different aspect ratios: From Figure 12, we can see that the ellipsoidal particles with small aspect ratio ($AR = 2$) always outperform those with large aspect ratio ($AR = 3$). Indeed, it is supported by both of the hydrodynamic collision and near wall dynamics results. First, from Figure 13, we can find in both of the shear rates, the ellipsoidal particles with small AR outperform those with large AR on either collision displacement or collision frequency. Second, in the results of near wall dynamics (c.f. Figure 15), the ellipsoidal particles with small AR manifest moving towards the wall, while those with large AR show the migration away from the wall. Thus the ellipsoidal particles with small AR have higher margination probability than those with large AR under the current shear rate regime we consider here.

As for the difference of margination probabilities among three kinds of MPs: sphere-like, oblate-like and prolate-like shown in

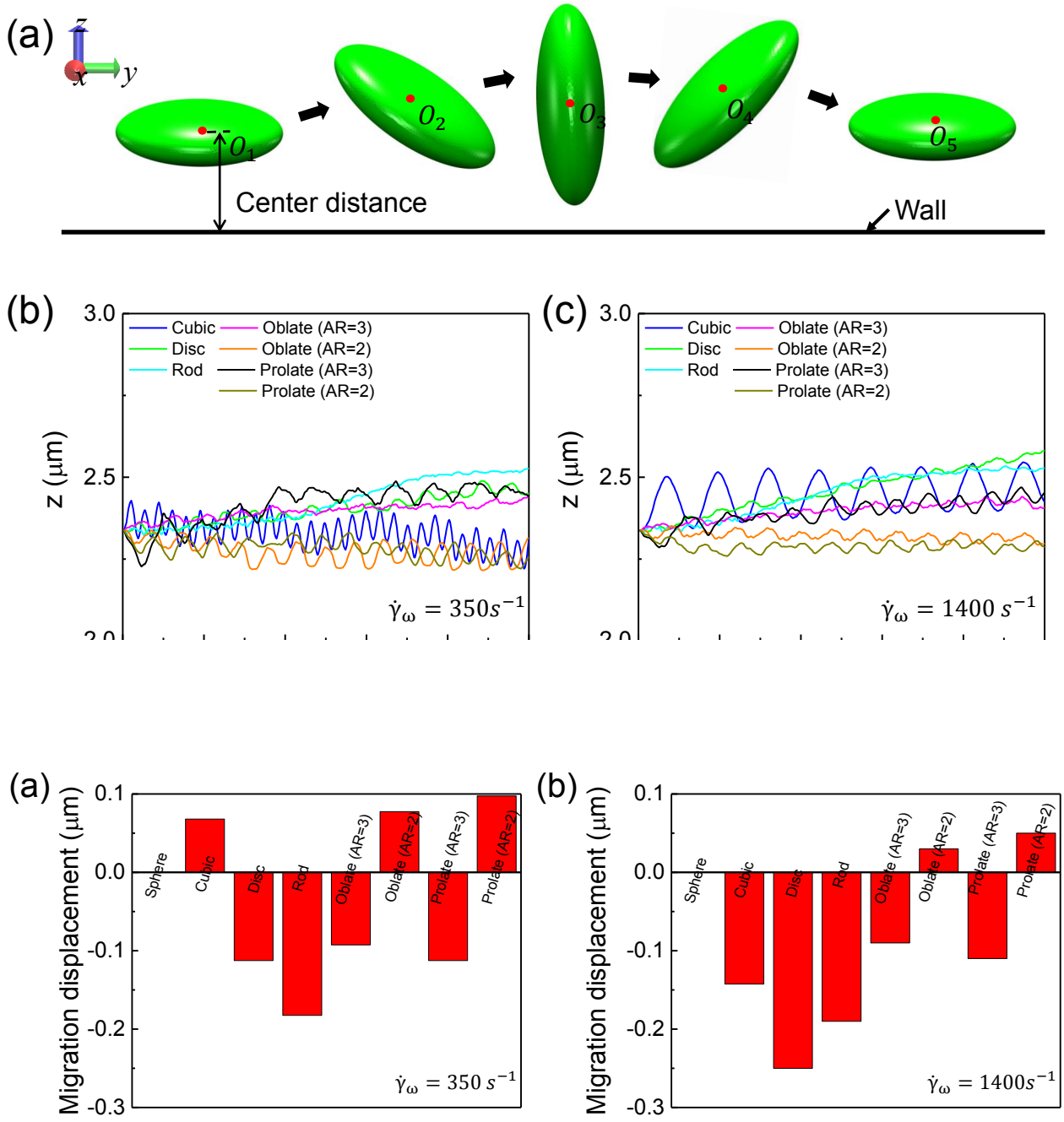

Fig. 15 Migration displacement of MPs under (a) $\dot{\gamma}_\omega = 350\ s^{-1}$ and (b) $\dot{\gamma}_\omega = 1400\ s^{-1}$. Positive value represents the moving towards the wall and negative value denotes the migration away from the wall.

Figure 11(d), we can only conclude that the sphere-like MP performs the best. No trend is found for the oblate-like and prolate-like MPs. We believe this is mainly induced by the larger collision frequency of sphere-like MPs. Though this finding is not consistent with some previous works[5,24], other numerical[26] and experimental[23] works confirmed our findings. For example, Vahidkhah *et al.*[24] presented that oblate particle showed the highest margination, and sphere was close behind, while the prolate performed the worst. This discrepancy may be induced by the hematocrit and size of the particles. The hematocrit in Vahidkhah *et al.*'s[24] work is about 24%, while in current work, it is 29%, which is larger. And current study has smaller size compared to that in Vahidkhah *et al.*'s[24] work (volume 7.238 μm^3 vs. 0.52 μm^3). Furthermore, they only consider one shear rate. This inconsistence further indicates the flow condition plays an important role in the margination of MPs. However, our findings are supported by the numerical results of Muller *et al.*[26]. They found that under the same shear rate, volume and hematocrit, the sphere particle outperforms the prolate particle on the margination behavior. Also, in experiments conducted by Thompson *et al.*[23], they found that under hematocrit 30%, the sphere with diameter 1 μm had higher accumulation near the wall than that of prolate particle

with $AR = 11$ under wall shear rate 1000 s^{-1}. One thing should be noted that in Thompson *et al.*'s[23] work, they also found that when increasing the size of the particle from 1 μm to 2 μm in diameter, though the sphere outperformed the prolate with $AR = 4$, the prolate with $AR = 9$ can exceed the sphere on the accumulation near the wall. This reveals that the margination of MPs also depends on the size of MPs, which confirms the inconsistence between current work and Vahidkhah *et al.*'s[24] work is partially attributed to the size of MPs.

To have an overall illustration of the interplay of shear rate and shape effects on the margination behavior of MPs, we plot all the results together and show them in Figure 16(a). For all of these different shaped MPs, the margination probabilities increase first and then keep approximately constant with the increment of shear rate. Thus, there exists a transitional shear rate region about 700 $s^{-1} < \dot{\gamma}_\omega < 900$ s^{-1}. If the shear rate is under this region, the margination strongly depends on the shear rate of the flow, and monotonically increases as the shear rate increases. While above it, the margination probability approaches plateau regime.

Although the margination behaviors of different shaped MPs have the same dependency on the shear rate, there is obvious difference among them. To reflect the shape effect, we compare the margination probabilities of MPs under different shear rates by introducing the surface area to volume ratio (SVR) to distinguish them. SVR is a more generic parameter to represent the shape of MPs. Figure 16(b) plots the margination probability contour on shear rate-SVR plane. We find that for blood flow with the same shear rate, the margination probability is not monotonic to SVR. While approximately there are two peaks at about SVR=6.4 μm^{-1} and SVR=7.1 μm^{-1} within regions of this study. Utilizing this contour map, we can predict the margination performance of particle with specific SVR. For example, the particle with SVR = 6.7 μm^{-1} under shear rate $\dot{\gamma}_\omega = 400$ s^{-1} is not considered here. But we can obtain the approximate margination probability which is about $0.56 \sim 0.67$.

However, the difference of margination probabilities for different shaped particles in current study is not very large. It reveals that changing the shape of particles under specific conditions such as hematocrit, size and shear rate, cannot significantly influence the margination. The findings in previous studies[22] accounting for the localization of particle on the wall should rely on the adhesion behavior like the adhesion frequency and contact area. Nevertheless, these simulation results can be potentially applied to guide the design of micro-drug carriers for biomedical applications.

4 Conclusion

In present work, we study the margination behaviors of different shaped MPs by developing an efficient multiscale numerical model. We calculate the margination probability of MPs with a statistically reliable method, upon obtaining the thickness of CFL under different shear rates. First, the shear rate dependent margination of sphere MP is investigated. It is found that when $\dot{\gamma}_\omega < 800$ s^{-1}, the margination probability dramatically increases with the increment of shear rate; while its growth rate decreases abruptly after $\dot{\gamma}_\omega$ exceeds 800 s^{-1}. This phenomenon is considered to be related with RBC structures in the blood flow. We find under low shear rate, RBCs aggregate together and rouleaux forms. This RBC structure results in large void spaces in the blood flow. Hence, the collision frequency of MPs with RBCs is small. However, with high shear rate, RBCs distribute more uniformly in the blood flow, the collision between MPs and RBCs becomes more frequent compared to that under low shear rate. Furthermore, the individual collision between a single RBC and a MP is examined. And we find that the collision displacement increases with the increment of the shear rate. Combining these two factors, MPs under high shear rate demonstrates stronger margination behavior due to higher collision frequency and larger collision displacement.

Further, the margination behaviors of sphere-like, oblate-like and prolate-like MPs under different shear rates are systematically investigated. We find that in addition to collision between RBCs and MPs, the near wall dynamics of MPs also plays a crucial role during MP margination. It should be noted that MPs that demonstrate poor performance at one process may stands out in another process. For example, under the low shear rate, the cubic marginates more readily than sphere, due to the high collision frequency and large collision displacement, and large migration displcement toward the wall. Nevertheless, under the high shear rate, the significant migration away from the wall for cubic MP results in lower margination than that of sphere, regardless of the better performance in collision process. In addition, we find that ellipsoidal MPs (oblate and prolate) with small AR have higher margination probabilities than those with large AR, regardless of the shear rate. It is attributed to their better performance in both the collision with RBCs and near wall dynamics. We should emphasize that the difference of margination probabilities for different shaped particles is not very large. It indicates that only changing shape of particles under specified conditions cannot effectively optimize drug carriers in terms of margination.

In conclusion, there exists a transition shear rate region 700 $s^{-1} < \dot{\gamma}_\omega < 900$ s^{-1} for different shaped MPs. Under it, the margination probabilities dramatically increase with the increment of shear rate; above it, the margination probabilities slowly increases, even keeps constant regardless of the change of shear rate. Finally, we plot a margination probability contour on the shear rate-SVR plane. It confirms the existence of transition shear rate and above results. The most important thing is that this contour can predict the margination probability of MPs under different shear rates, which are not considered in this work. Thus, it can offer the guidance to design MP-based drug carriers for different biomedical applications, where different margination behaviors are needed.

Acknowledgment

This work was supported by National Science Foundation (OAC-1755779). Z. S., H. Y. and Y. L. are grateful for the support from Department of Mechanical Engineering at the University of Connecticut. Z. S. and H. Y. acknowledge the partial financial supports from the GE Fellowship for Innovation. This research benefited in part from the computational resources and staff contri-

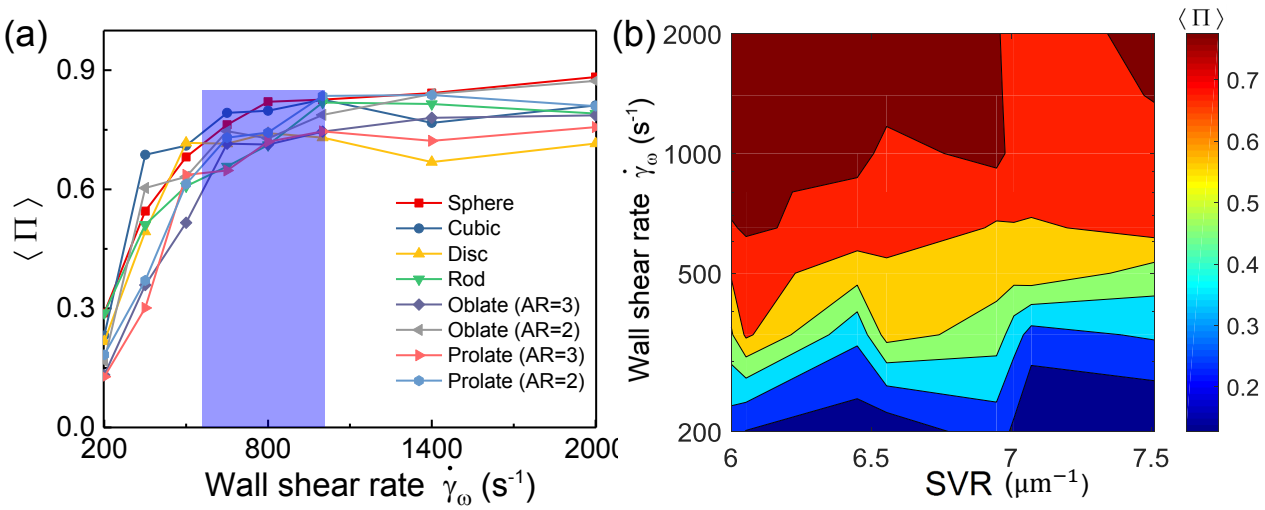

Fig. 16 (a) Margination probabilities against shear rate for different shaped MPs. (b) Contour of margination probability on the shear rate-SVR plane.

butions provided by the Booth Engineering Center for Advanced Technology (BECAT) at the University of Connecticut. Part of this work used the Extreme Science and Engineering Discovery Environment (XSEDE), which is supported by the National Science Foundation grant number ACI-1053575.

Notes and references

1 J. Shi, P. W. Kantoff, R. Wooster and O. C. Farokhzad, *Nat. Rev. Cancer*, 2017, **17**, 20.

2 O. Veiseh, J. W. Gunn and M. Zhang, *Adv. Drug Delivery Rev.*, 2010, **62**, 284–304.

3 E. Tasciotti, X. Liu, R. Bhavane, K. Plant, A. D. Leonard, B. K. Price, M. M.-C. Cheng, P. Decuzzi, J. M. Tour, F. Robertson *et al.*, *Nature nanotechnology*, 2008, **3**, 151.

4 J. S. Ananta, B. Godin, R. Sethi, L. Moriggi, X. Liu, R. E. Serda, R. Krishnamurthy, R. Muthupillai, R. D. Bolskar, L. Helm *et al.*, *Nature nanotechnology*, 2010, **5**, 815.

5 P. Decuzzi, B. Godin, T. Tanaka, S.-Y. Lee, C. Chiappini, X. Liu and M. Ferrari, *J. Controlled Release*, 2010, **141**, 320–327.

6 W. H. De Jong, W. I. Hagens, P. Krystek, M. C. Burger, A. J. Sips and R. E. Geertsma, *Biomaterials*, 2008, **29**, 1912–1919.

7 R. H. Muller and C. M. Keck, *J. Biotechnol.*, 2004, **113**, 151–170.

8 P. Decuzzi, R. Pasqualini, W. Arap and M. Ferrari, *Pharmaceutical research*, 2009, **26**, 235.

9 P. Decuzzi and M. Ferrari, *Biomaterials*, 2008, **29**, 377–384.

10 Y. Li, Y. Lian, L. T. Zhang, S. M. Aldousari, H. S. Hedia, S. A. Asiri and W. K. Liu, *Interface focus*, 2016, **6**, 20150086.

11 H. Ye, Z. Shen, L. Yu, M. Wei and Y. Li, *Proc. R. Soc. A*, 2018, **474**, 20170845.

12 J. P. Best, Y. Yan and F. Caruso, *Adv. Healthcare Mater.*, 2012, **1**, 35–47.

13 Y. Liu, J. Tan, A. Thomas, D. Ou-Yang and V. R. Muzykantov, *Therapeutic delivery*, 2012, **3**, 181–194.

14 L. Tao, W. Hu, Y. Liu, G. Huang, B. D. Sumer and J. Gao, *Experimental Biology and Medicine*, 2011, **236**, 20–29.

15 F. Gentile, C. Chiappini, D. Fine, R. Bhavane, M. Peluccio, M. M.-C. Cheng, X. Liu, M. Ferrari and P. Decuzzi, *Journal of biomechanics*, 2008, **41**, 2312–2318.

16 R. Toy, E. Hayden, C. Shoup, H. Baskaran and E. Karathanasis, *Nanotechnology*, 2011, **22**, 115101.

17 S.-Y. Lee, M. Ferrari and P. Decuzzi, *Nanotechnology*, 2009, **20**, 495101.

18 J. Tan, A. Thomas and Y. Liu, *Soft Matter*, 2012, **8**, 1934–1946.

19 T.-R. Lee, M. Choi, A. M. Kopacz, S.-H. Yun, W. K. Liu and P. Decuzzi, *Scientific reports*, 2013, **3**, 2079.

20 A. Tokarev, A. Butylin and F. Ataullakhanov, *Biophys. J.*, 2011, **100**, 799–808.

21 B. Godin, C. Chiappini, S. Srinivasan, J. F. Alexander, K. Yokoi, M. Ferrari, P. Decuzzi and X. Liu, *Advanced functional materials*, 2012, **22**, 4225–4235.

22 A. L. Van De Ven, P. Kim, J. R. Fakhoury, G. Adriani, J. Schmulen, P. Moloney, F. Hussain, M. Ferrari, X. Liu, S.-H. Yun *et al.*, *J. Controlled Release*, 2012, **158**, 148–155.

23 A. J. Thompson, E. M. Mastria and O. Eniola-Adefeso, *Biomaterials*, 2013, **34**, 5863–5871.

24 K. Vahidkhah and P. Bagchi, *Soft Matter*, 2015, **11**, 2097–2109.

25 D. A. Reasor, M. Mehrabadi, D. N. Ku and C. K. Aidun, *Ann. Biomed. Eng.*, 2013, **41**, 238–249.

26 K. Müller, D. A. Fedosov and G. Gompper, *Sci. Rep.*, 2014, **4**, 4871.

27 A. W. Tilles and E. C. Eckstein, *Microvasc. Res.*, 1987, **33**, 211–223.

28 E. C. Eckstein, A. W. Tilles and F. J. Millero III, *Microvasc. Res.*, 1988, **36**, 31–39.

29 R. Fåhræus and T. Lindqvist, *Am. J. Physiol.*, 1931, **96**, 562–568.

30 T. G. Papaioannou and C. Stefanadis, *Hellenic J. Cardiol.*, 2005, **46**, 9–15.

31 S. Chen and G. D. Doolen, *Annu. Rev. Fluid Mech.*, 1998, **30**,

329–364.
32 F. Mackay, S. T. Ollila and C. Denniston, *Comput. Phys. Commun.*, 2013, **184**, 2021–2031.
33 Z. Guo, C. Zheng and B. Shi, *Phys. Rev. E*, 2002, **65**, 046308.
34 S. Plimpton, *J. Comput. Phys.*, 1995, **117**, 1–19.
35 D. A. Fedosov, B. Caswell and G. E. Karniadakis, *Biophys. J.*, 2010, **98**, 2215–2225.
36 D. A. Fedosov, W. Pan, B. Caswell, G. Gompper and G. E. Karniadakis, *Proc. Natl. Acad. Sci. U.S.A.*, 2011, **108**, 11772–11777.
37 M. P. Allen and D. J. Tildesley, *Computer simulation of liquids*, Oxford university press, 1989.
38 M. Dao, J. Li and S. Suresh, *Mater. Sci. Eng. C*, 2006, **26**, 1232–1244.
39 H. Ye, Z. Shen, L. Yu, M. Wei and Y. Li, *ACS Biomater. Sci. Eng.*, 2018, **4**, 66–77.
40 H. Ye, Z. Shen and Y. Li, *Computational Mechanics*, 2017.
41 Y. Liu and W. K. Liu, *J. Comput. Phys.*, 2006, **220**, 139–154.
42 C. S. Peskin, *J. Comput. Phys.*, 1972, **10**, 252–271.
43 C. S. Peskin, *Acta Numer.*, 2002, **11**, 479–517.
44 T. Krüger, F. Varnik and D. Raabe, *Comput. Math. Appl.*, 2011, **61**, 3485–3505.
45 Z.-G. Feng and E. E. Michaelides, *J. Comput. Phys.*, 2004, **195**, 602–628.
46 H. Ye, H. Wei, H. Huang and X.-y. Lu, *Phys. Fluids*, 2017, **29**, 021902.
47 P.-O. Persson and G. Strang, *SIAM review*, 2004, **46**, 329–345.
48 P.-O. Persson, *PhD thesis*, Massachusetts Institute of Technology, 2005.
49 R. M. MacMECCAN, J. Clausen, G. Neitzel and C. Aidun, *J. Fluid Mech.*, 2009, **618**, 13.
50 R. Mittal and G. Iaccarino, *Annu. Rev. Fluid Mech.*, 2005, **37**, 239–261.
51 D. A. Fedosov, B. Caswell, A. S. Popel and G. E. Karniadakis, *Microcirculation*, 2010, **17**, 615–628.
52 J. B. Freund and M. Orescanin, *J. Fluid Mech.*, 2011, **671**, 466–490.
53 S. Kim, R. L. Kong, A. S. Popel, M. Intaglietta and P. C. Johnson, *Am. J. Physiol. Heart Circ. Physiol.*, 2007, **293**, H1526–H1535.
54 M. Abkarian, C. Lartigue and A. Viallat, *Phys. Rev. Lett.*, 2002, **88**, 068103.
55 A. Farutin and C. Misbah, *Phys. Rev. Lett.*, 2013, **110**, 108104.
56 A. Kumar and M. D. Graham, *Phys. Rev. Lett.*, 2012, **109**, 108102.
57 H. Zhao, E. S. Shaqfeh and V. Narsimhan, *Phys. Fluids*, 2012, **24**, 011902.
58 H. Zhao and E. S. Shaqfeh, *Phys. Rev. E*, 2011, **83**, 061924.
59 J. Zhang, P. C. Johnson and A. S. Popel, *J. Biomech.*, 2008, **41**, 47–55.
60 D. A. Fedosov, M. Dao, G. E. Karniadakis and S. Suresh, *Ann. Biomed. Eng.*, 2014, **42**, 368–387.
61 A. Kumar and M. D. Graham, *Phys. Rev. E*, 2011, **84**, 066316.
62 R. K. Singh and K. Sarkar, *Phys. Rev. E*, 2015, **92**, 063029.
63 A. Kumar and M. D. Graham, *Soft Matter*, 2012, **8**, 10536–10548.
64 V. Narsimhan, H. Zhao and E. S. Shaqfeh, *Phys. Fluids*, 2013, **25**, 061901.
65 R. G. H. Rivera, X. Zhang and M. D. Graham, *Phys. Rev. Fluids*, 2016, **1**, 060501.